



HD 89345: A bright oscillating star hosting a transiting warm Saturn-sized planet observed by K2

Downloaded from: <https://research.chalmers.se>, 2025-12-08 23:28 UTC

Citation for the original published paper (version of record):

Van Eylen, V., Dai, F., Mathur, S. et al (2018). HD 89345: A bright oscillating star hosting a transiting warm Saturn-sized planet observed by K2. *Monthly Notices of the Royal Astronomical Society*, 478(4): 4866-4880. <http://dx.doi.org/10.1093/mnras/sty1390>

N.B. When citing this work, cite the original published paper.

HD 89345: a bright oscillating star hosting a transiting warm Saturn-sized planet observed by K2

V. Van Eylen,^{1★} F. Dai,^{2,3} S. Mathur,^{4,5} D. Gandolfi,⁶ S. Albrecht,⁷ M. Fridlund,^{1,8}
R. A. García,^{9,10} E. Guenther,¹¹ M. Hjorth,⁷ A. B. Justesen,⁷ J. Livingston,¹²
M. N. Lund,⁷ F. Pérez Hernández,^{4,5} J. Prieto-Arranz,^{4,5} C. Regulo,^{4,5} L. Bugnet,^{9,10}
M. E. Everett,¹³ T. Hirano,¹⁴ D. Nespral,^{4,5} G. Nowak,^{4,5} E. Palle,^{4,5} V. Silva Aguirre,⁷
T. Trifonov,¹⁵ J. N. Winn,³ O. Barragán,⁶ P. G. Beck,^{4,5} W. J. Chaplin,^{7,16}
W. D. Cochran,¹⁷ S. Csizmadia,¹⁸ H. Deeg,^{4,5} M. Endl,¹⁷ P. Heeren,¹⁹ S. Grziwa,²⁰
A. P. Hatzes,¹¹ D. Hidalgo,^{4,5} J. Korth,²⁰ S. Mathis,^{9,10} P. Montañes Rodriguez,^{4,5}
N. Narita,^{12,21,22} M. Patzold,²⁰ C. M. Persson,⁸ F. Rodler²³ and A. M. S. Smith¹⁸

Affiliations are listed at the end of the paper

Accepted 2018 May 4. Received 2018 May 2; in original form 2018 February 23

ABSTRACT

We report the discovery and characterization of HD 89345b (K2-234b; EPIC 248777106b), a Saturn-sized planet orbiting a slightly evolved star. HD 89345 is a bright star ($V = 9.3$ mag) observed by the K2 mission with 1 min time sampling. It exhibits solar-like oscillations. We conducted asteroseismology to determine the parameters of the star, finding the mass and radius to be $1.12^{+0.04}_{-0.01} M_{\odot}$ and $1.657^{+0.020}_{-0.004} R_{\odot}$, respectively. The star appears to have recently left the main sequence, based on the inferred age, $9.4^{+0.4}_{-1.3}$ Gyr, and the non-detection of mixed modes. The star hosts a ‘warm Saturn’ ($P = 11.8$ d, $R_p = 6.86 \pm 0.14 R_{\oplus}$). Radial-velocity follow-up observations performed with the Fibre-fed Echelle Spectrograph, HARPS, and HARPS-N spectrographs show that the planet has a mass of $35.7 \pm 3.3 M_{\oplus}$. The data also show that the planet’s orbit is eccentric ($e \approx 0.2$). An investigation of the rotational splitting of the oscillation frequencies of the star yields no conclusive evidence on the stellar inclination angle. We further obtained Rossiter–McLaughlin observations, which result in a broad posterior of the stellar obliquity. The planet seems to confirm to the same patterns that have been observed for other sub-Saturns regarding planet mass and multiplicity, orbital eccentricity, and stellar metallicity.

Key words: asteroseismology – planets and satellites: composition – planets and satellites: formation – planets and satellites: fundamental parameters.

1 INTRODUCTION

When a planet transits, this opens up a potential window for dynamical studies (through e.g. the measurement of stellar obliquities) as well as atmospheric studies (through e.g. transmission spectroscopy), but unfortunately many host stars are too faint for these type of studies to be feasible.

We report the discovery and characterization of HD 89345b (K2-234b; EPIC 248777106b), a newly discovered transiting planet orbiting a bright star ($V = 9.3$), which was observed by the K2 mission

(Howell et al. 2014).¹ This is a warm sub-Saturn planet. Such planets, with a size between Uranus and Neptune, do not exist in the Solar system. They exhibit a wide variety of masses and their formation is not fully understood (Petigura et al. 2017).

We confirm the existence of the planet and measure its mass with radial-velocity measurements, using the Fibre-fed Echelle Spectrograph (FIES) (Telting et al. 2014), HARPS (Mayor et al. 2003), and HARPS-N (Cosentino et al. 2012) spectrographs. This work was done within the KESPRINT collaboration (see e.g. Sanchis-Ojeda

¹During the reviewing stage of this manuscript, another manuscript independently reporting on this system was made publicly available (Yu et al. 2018).

★ E-mail: vaneylen@strw.leidenuniv.nl

et al. 2015; Van Eylen et al. 2016a,b; Fridlund et al. 2017; Gandolfi et al. 2017; Smith et al. 2018). We determine accurate stellar parameters from asteroseismology, through the analysis of stellar oscillations that are seen in the K2 light curve.

In Section 2, we describe the observations of this system, including the K2 observations, high-resolution imaging, and spectroscopic observations. In Section 3, we describe the derivation of spectroscopic stellar parameters, and the asteroseismic analysis of the star. In Section 4, we derive the properties of the planet and its orbit. We conclude with a discussion in Section 5.

2 OBSERVATIONS

2.1 K2 photometry

HD 89345 was observed by the K2 mission (Howell et al. 2014) during Campaign 14 (UT 2017 May 31 to Aug 19). As a bright ($V = 9.3$ mag) solar-type sub-giant star, HD 89345 was proposed as a short-cadence (with an integration time of 58.8 s) target to enable an asteroseismic analysis (Lund et al., guest observer program GO14010). We downloaded the target pixel files from the Mikulski Archive for Space Telescopes.² We first removed the systematic flux variation due to the rolling motion of the *Kepler* spacecraft. We adopted a similar procedure to that described by Vanderburg & Johnson (2014). In short, we put down a circular aperture around the brightest pixel in the target pixel files. We then fitted a two-dimensional Gaussian function to the flux distribution within the aperture. The x and y positions of the Gaussian functions were used as tracers of the spacecraft's rolling motion. We fitted a piecewise linear function between the aperture-summed flux variation and the x and y positions. This function describes the systematic variation due to the rolling motion and was removed by division.

Prior to our transit detection, we removed any long-term astrophysical or instrumental flux variation by fitting a cubic spline to the light curve. We then searched the resultant light curves for periodic transit signals using the Box-Least-Square algorithm (Kovács, Zucker & Mazeh 2002). The signal of planet b was clearly detected with a signal-to-noise ratio (SNR) of 16. We searched for additional transiting planets after removing the transits of planet b. No additional signal was detected with $\text{SNR} > 4.5$.

2.2 High-resolution photometry

We conducted speckle-interferometry observations of the host star using the NASA Exoplanet Star and Speckle Imager (NESSI; Scott, Howell & Horch 2016; Scott et al., in preparation.) on the WIYN 3.5 m telescope. The observations were conducted at 562 and 832 nm simultaneously, using high-speed electron-multiplying CCDs with individual exposure times of 40 ms. The data were collected and reduced following the procedures described by Howell et al. (2011), resulting in reconstructed 4.6×4.6 arcsec images of the host star with a resolution close to the diffraction limit. We did not detect any secondary sources in the reconstructed images. We produced smooth contrast curves from the reconstructed images by fitting a cubic spline to the 5σ sensitivity limits within a series of concentric annuli. The achieved contrast of 5 mag at 0.2 arcsec strongly constrains the possibility that a nearby faint star is the source of the observed transit signal. We show the reconstructed

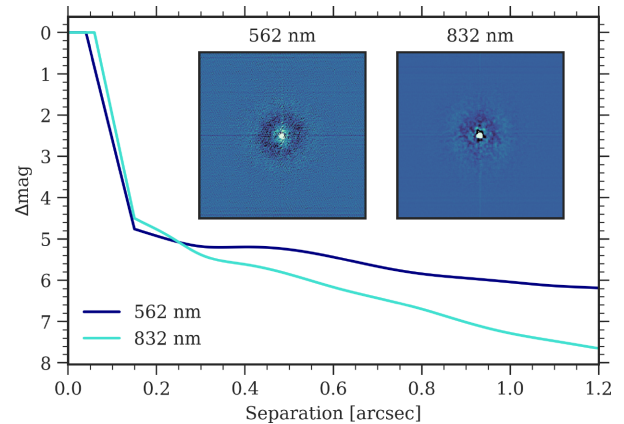


Figure 1. NESSI speckle-interferometric observations of HD 89345 at 562 and 832 nm reveal no nearby stars. Contrast limits as a function of angular separation are shown (see Section 2.2 for details). The inset images have a scale of 4.6×4.6 arcsec, and are oriented with northeast in the upper left.

images and the resulting background source sensitivity limits in Fig. 1.

2.3 Spectroscopic observations

High-resolution spectroscopic observations of HD 89345 were obtained between 2017 December 23 and 2018 March 25, using three different spectrographs.

Following the observing strategy described by Gandolfi et al. (2013), we gathered 16 high-resolution spectra ($R = 67\,000$) of HD 89345 with the FIES (Frandsen & Lindberg 1999; Telting et al. 2014) mounted at the 2.56 m Nordic Optical Telescope (NOT) of Roque de los Muchachos Observatory (La Palma, Spain). The observations were carried out as part of our K2 follow-up programs 2017B/059, 56-209, and 56-010. We reduced the data using standard image reduction and analysis facility (IRAF) and interactive data language (IDL) routines and extracted the RVs via multi-order cross-correlations against the stellar spectrum with the highest SNR as a template.

We also acquired 38 spectra (program ID 0100.C-0808) with the HARPS spectrograph ($R \approx 115\,000$; Mayor et al. 2003) mounted at the ESO-3.6 m telescope of La Silla observatory (Chile), as well as 12 spectra (program IDs 2017B/059, A36TAC_12, and CAT17B_99) with the HARPS-N spectrograph ($R \approx 115\,000$; Cosentino et al. 2012) mounted at the 3.6 m Telescopio Nazionale Galileo (TNG) of Roque de los Muchachos Observatory. To account for possible RV drifts of the instruments, we used the simultaneous Fabry Perot calibrator. In the attempt to measure the sky-project spin-orbit angle, λ , 21 HARPS spectra were gathered during the transit occurring on the night 2018 February 23/24. We reduced the data using the dedicated offline HARPS and HARPS-N pipelines and extracted the RVs via cross-correlation with a numerical mask for a G2 type star.

In order to detect the transiting planet in the Doppler observations and exclude false positive scenarios (e.g. a background binary), we performed a frequency analysis of the RVs and their activity indicators (BIS and FWHM). On epochs 2458 129 and 2458 140, we collected FIES and HARPS-N spectra of HD 89345 within about 1 h. Similarly, on epochs 2458 143 and 2458 144, we obtained FIES and HARPS data within about 2 h. We used these measurements to estimate the offsets of the RV, FWHM, BIS between the instruments and calculate the periodograms of the combined data. These

²<https://archive.stsci.edu/k2>.

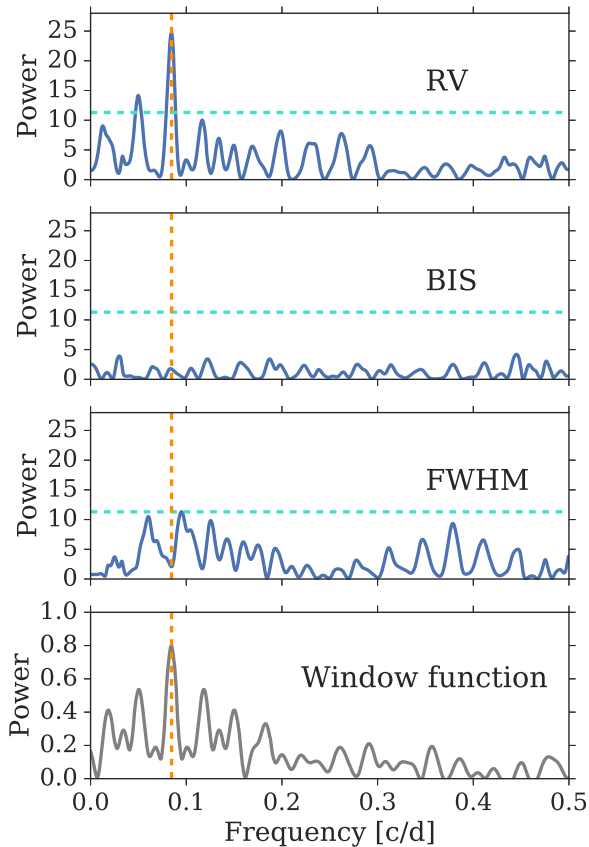


Figure 2. Generalized Lomb–Scargle periodogram of the RV, BIS, and FWHM measurements for the combined FIES, HARPS, and HARPS-N observations, respectively, and the window function centered at the orbital frequency of the transiting planet. The RV peak at the orbital period observed from transit observations (vertical orange dotted line) does not have a corresponding BLS or FWHM peak, suggesting that it is induced by the planet. The light blue dotted horizontal line indicates a 0.01 per cent false alarm probability.

offsets have only been used to perform the frequency analysis. For the procedure of the joint RV modelling, we refer the reader to Section 4.

The first three panels of Fig. 2 display the generalized Lomb–Scargle periodograms (Zechmeister & Kürster 2009) of the combined RV, BIS, and FWHM measurements. The dashed vertical line marks the orbital frequency of the transiting planet, whereas the horizontal lines represent the 0.01 per cent false-alarm probability (FAP). We determined the FAP following the Monte Carlo bootstrap method described in Kuerster et al. (1997). In the last panel, we show the GLS of the window function shifted to the right by 0.085 c/d (i.e. the orbital frequency of the transiting planet), and mirrored to the left of this frequency, to facilitate visual identification of possible aliases.

The periodogram of the RV measurements has a strong peak at the orbital frequency of the transiting planet with a FAP \ll 0.01 per cent, implying that we would infer the presence of the transiting planet even in the absence of K2 photometry. This peak has no counterparts in the periodograms of the BIS and FWHM, suggesting that the observed RV variation is induced by the transiting planet. We note the periodogram of the RV displays peaks separated by about 0.034 c/d, which corresponds to about 30 d. Those peaks are aliases of the planet’s frequency and are due to the fact that our observa-

tions have been performed around new moon to avoid contamination from the scattered Sun light.

All RV data points and their observation times are listed in Table A1, along with the BIS, FWHM, exposure times, and SNR per pixel at 5500 Å. For the HARPS and HARPS-N data, we also report the activity index $\log R'_{\text{HK}}$ of the Ca II H & K lines.

3 STELLAR PARAMETERS

We determined the stellar parameters based on spectroscopy, parallax and magnitude measurements, and asteroseismology. Below we describe each of these methods. We also investigated the inclination angle of the star based on rotational splittings of the oscillation modes.

3.1 Spectroscopic analysis

In order to derive the stellar parameters, we combined all the HARPS spectra (see Section 2.3) to form a co-added spectrum with a SNR of about 500 per pixel at 5500 Å. This was analysed using the spectral analysis package Spectroscopy Made Easy (SME, Valenti & Piskunov 1996; Valenti & Fischer 2005; Piskunov & Valenti 2017). SME calculates synthetic spectra in local thermodynamic equilibrium (LTE) for a set of given stellar parameters and fits them to observed high-resolution spectra using a χ^2 minimization procedure. We used SME version 5.2.2 and a grid of the ATLAS12 model atmospheres (Kurucz 2013), which is a set of one-dimensional (1D) models applicable to solar-like stars. We then fitted the observed spectrum to this grid of theoretical ATLAS12 model atmospheres, selecting parts of the observed spectrum that contain spectral features that are sensitive to the required parameters. We used the empirical calibration equations for solar-like stars from Bruntt et al. (2010), in order to determine the micro-turbulent and macro-turbulent velocities, respectively. We then followed the procedure in Fridlund et al. (2017). In short, we used the wings of the hydrogen Balmer lines to determine the effective temperature, T_{eff} (Fuhrmann, Axer & Gehren 1993, 1994). The line cores were excluded in this fitting procedure due to their origin in layers above the photosphere.

The stellar surface gravity, $\log g_*$, was estimated from the wings of the Ca I 6102, 6122, 6162 triplet, and the Ca I 6439 Å line. We separately determined $\log g_*$ from the Mg I 5167, 5172, 5183 triplet and found a result consistent within 1σ . We conservatively adopted the value from Mg I, which has the highest uncertainty.

The projected stellar rotational velocity, $v \sin i$, and the metal abundances, were measured by fitting the profile of several tens of clean and unblended metal lines. The final model was checked with the Na doublet (5889 and 5896 Å). The velocity profile of the absorption lines have a degeneracy caused by the combination of the macro turbulence (V_{mac}) and the rotational velocity component, $v \sin i$. Although there are theoretical models for V_{mac} , empirical calibrations have been made by Bruntt et al. (2010) and Doyle et al. (2014). Both use a combination of spectroscopic and asteroseismic analysis in order to correlate macro turbulence and rotation for a sample of about 50 stars. While the number of stars in each sample (about 25) is relatively small, together they demonstrate clearly empirical trends which can be used to assign a value to V_{mac} after T_{eff} has been determined. In the case of this star, there is a small difference between both calibrations. The relation by Bruntt et al. (2010) indicates $V_{\text{mac}} = 1.7 \pm 0.4 \text{ km s}^{-1}$, while using the relation of Doyle et al. (2014) results in $V_{\text{mac}} = 3.51 \pm 0.5 \text{ km s}^{-1}$. This leads to $v \sin i$ of 3.45 ± 0.50 and $2.60 \pm 0.50 \text{ km s}^{-1}$, respectively, for the two values of V_{mac} . Here, we adopt the calibration by Doyle et al.

Table 1. Spectroscopic parameters (see Section 3.1).

Parameter	Value
Effective temperature, T_{eff} (K)	5420 ± 110
Surface gravity from Mg I, $\log g$ (cgs)	3.85 ± 0.20
Surface gravity from Ca I, $\log g$ (cgs)	3.85 ± 0.13
Metallicity, [Fe/H]	0.45 ± 0.05
Projected rotation speed, $v \sin i$ (km s $^{-1}$)	2.60 ± 0.50
Microturbulence (km s $^{-1}$)	0.80 ± 0.10
Macroturbulence (km s $^{-1}$)	3.51 ± 0.50

Table 2. We list the *Gaia* parallax measurement, as well as magnitude measurements in different colours, and the stellar parameters, we derived from these observations (see Section 3.2).

Parameter	Value	Source
Paral. [mas]	7.527 ± 0.046	Gaia Collaboration (2018)
<i>B</i> Mag.	10.15 ± 0.04	Høg et al. (2000)
<i>V</i> Mag.	9.38 ± 0.03	Høg et al. (2000)
<i>G</i> Mag.	9.159 ± 0.001	Gaia Collaboration (2016b)
<i>J</i> Mag.	8.091 ± 0.020	Cutri et al. (2003)
<i>H</i> Mag.	7.766 ± 0.040	Cutri et al. (2003)
<i>K</i> Mag.	7.721 ± 0.018	Cutri et al. (2003)
R [R_{\odot}]	$1.78^{+0.06}_{-0.06}$	This work
M [M_{\odot}]	$1.10^{+0.06}_{-0.14}$	This work
L [L_{\odot}]	$2.71^{+0.12}_{-0.12}$	This work

(2014) for two reasons. First, the treatment of the asteroseismic data is more thorough in this work, since it had access to high-quality data from the *Kepler* space mission, which allowed them to dig deeper into the rotational aspects of the target stars. Secondly, the values for the empirical sample of Bruntt et al. (2010) tend to be lower than values by Doyle et al. (2014), but also lower than data by Gray (1984) and Valenti & Fischer (2005). The latter used the SME modelling tool, that we have also used to interpret our spectroscopic data here. Finally, we note that the lower $v \sin i$ value is also more consistent with limits derived from in-transit spectroscopic observations (see Section 3.4.2).

All spectroscopic parameters are listed in Table 1.

3.2 Parallax measurements

We use the parallax and the observed apparent magnitudes to obtain an independent estimate of the stellar parameters. This was done using BASTA (Silva Aguirre et al. 2015) with a grid of BaSTI isochrones (Pietrinferni et al. 2004). The BaSTI isochrones contain synthetic colours and absolute magnitudes in a range of photometric broad-band filters. Using the *Gaia* parallax (see table 2 Gaia Collaboration 2016a, 2018), we convert apparent magnitudes to absolute magnitudes. Following Luri et al. (2018), we add 0.1 mas in quadrature to the uncertainty of the parallax, to account for systematic uncertainty. We estimate the reddening $E(B - V)$ along the line of sight using the Green et al. (2015) dust map and transform $E(B - V)$ to extinction A_{λ} in different filters following Casagrande & VandenBerg (2014). The extinction-corrected absolute magnitudes are fitted to the grid of isochrones following the Bayesian grid-modelling approach employed by BASTA. We fitted the Johnson *V* and *B* magnitudes as well as 2MASS *J*, *H*, and *K* magnitudes and derive the stellar luminosity, mass, and radius. All parameters are listed in Table 2.

3.3 Asteroseismic analysis

We subsequently determined stellar parameters using asteroseismology. The A2Z pipeline (Mathur et al. 2010) was used on the reduced K2 photometry (see Section 2.1), after excising the data obtained during transits. The pipeline determines the global seismic parameters $\Delta\nu$, the mean large frequency spacing, and ν_{max} , the frequency of maximum power. The first parameter is given by the distance in frequency between two modes of the same angular degree and of consecutive orders, a quantity which is proportional to the square root of the mean density of the star (Kjeldsen & Bedding 1995). The frequency of maximum power is related to the cut-off frequency, which is directly proportional to the surface gravity of the star (Brown et al. 2011). This resulted in a first estimate of the global seismic parameters for this star: $\Delta\nu = 67.00 \pm 1.87 \mu\text{Hz}$ and $\nu_{\text{max}} = 1300 \pm 58 \mu\text{Hz}$.

We determined the set of individual *p*-mode frequencies using two methods. The first method involves maximum *a priori* (MAP) fitting. To reduce the number of free parameters, all the modes with $l = 0$, $l = 1$, and $l = 2$ were fitted together (Roca Cortés et al. 1999), assuming one single Lorentzian profile per mode (without accounting for any rotation), a constant line width and amplitude per order, and constant visibilities between the modes (1, 1.5, and 0.5, respectively, for $l = 0$, 1, and 2). To validate this last assumption, we also fitted the data leaving the visibilities as free parameters, and found that the result of this fit agrees with the constant visibilities to within the uncertainties, as do the fitted mode frequencies. The K2 photometry used in this analysis was treated with the KADASC correction pipeline (García et al. 2011). The transits were removed and the data were interpolated using inpainting methods (García et al. 2014a; Pires et al. 2015).

The second frequency extraction method uses the Bayesian methodology outlined by Lund et al. (2017), which was applied to data prepared using the K2P² pipeline to extract and correct the K2 photometry in a way that is optimal for determining oscillation frequencies (Lund et al. 2014, 2016).

The frequencies of these two methods agree to within the estimated 1σ uncertainties for all frequencies. The MAP fitting identified additional low-amplitude frequency detections. We adopt the frequencies provided by the Bayesian method for the modelling, because this methodology provide access to the posterior probabilities of each fitted parameter. A power spectrum of the K2 photometry is shown in Fig. 3, together with the detected Bayesian frequencies. We list all frequencies in Table A2.

We subsequently modeled the oscillation frequencies following two different approaches. The first stellar modelling method makes use of the MESA evolution code (Paxton et al. 2011). The OPAL opacities (Iglesias & Rogers 1996), the GS98 metallicity mixture (Grevesse & Sauval 1998), and the exponential prescription of Herwig (2000) for the overshooting were used, and otherwise the standard input physics from MESA was applied. The frequencies of the acoustic modes were calculated with the ADIPLS code (Christensen-Dalsgaard 2008) in the adiabatic approximation. A χ^2 minimization including *p*-mode frequencies and spectroscopic data was applied to a grid of models. The general procedure is described in Pérez Hernández et al. (2016). However, since HD 89345 is a subgiant star with eigenfrequencies approximately in the asymptotic *p*-mode regime, all the modes given in Table A2 were fitted simultaneously with weights based on their observational errors and the same surface correction was applied to all the modes, i.e. a second order polynomial fit to the relative differences $I_{nl}\delta\omega_{nl}/\omega_{nl}$, where I_{nl} is the dimensionless energy (see Pérez Hernández et al. 2016; for more

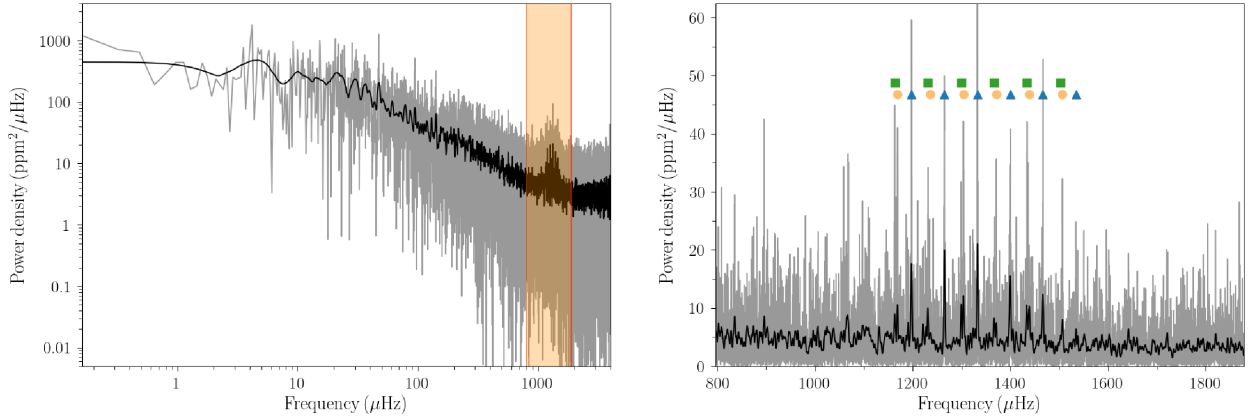


Figure 3. Power spectrum density of HD 89345, showing a power excess due to stellar oscillations, based on the K2 photometry. The right-hand panel is a zoom-in on the region with solar-like oscillations. The power spectrum is shown in grey and a smoothed version is shown in black. The colour symbols indicate the derived frequencies as listed in Table A2.

Table 3. Stellar parameters derived from asteroseismic modelling using two different approaches (see Section 3.3).

Parameter	MESA	BASTA
$R [R_{\odot}]$	1.657 ± 0.017	$1.657^{+0.02}_{-0.004}$
$M [M_{\odot}]$	1.11 ± 0.04	$1.120^{+0.04}_{-0.01}$
$\rho [\text{g/cm}^3]$	0.3413 ± 0.0010	0.343 ± 0.002
$T_{\text{eff}} [\text{K}]$	5480 ± 100	5499 ± 73
$L [L_{\odot}]$	2.21 ± 0.22	$2.27^{+0.21}_{-0.14}$
Age [Gyr]	8.3 ± 1.2	$9.4^{+0.4}_{-1.3}$
$\log g [\text{dex}]$	4.045 ± 0.007	$4.044^{+0.006}_{-0.004}$
α	1.53 ± 0.06	1.7917 (fixed)
f_{ov}	0.004 ± 0.007	0 (fixed)

details). The input spectroscopic parameters considered were the effective temperature, surface gravity, and metallicity (see Table 1). The grid is composed of evolution sequences with stellar masses (M_*) from 0.95 to 1.25 M_{\odot} with a step of $\Delta M = 0.01 M_{\odot}$, initial metallicities (Z_{ini}) from 0.002 to 0.04 with a step of $\Delta Z = 1/300$, mixing length parameters (α) from 1.5 to 2.2 and step $\Delta\alpha = 0.1$ and overshooting parameter f_{ov} from 0 to 0.04 and step of 0.01. The helium abundance was constrained by adopting a Galactic chemical evolution model with $\Delta Z/\Delta Y = 1.4$.

To estimate the uncertainty in the output parameters, we assumed normally distributed uncertainties for the observed frequencies, for the mean value of $I_n \delta\omega/\omega$ for radial oscillations and for the spectroscopic parameters. We then search for the model with the minimum χ^2 in every realization, and report mean and 1σ uncertainty values in Table 3.

In the second approach, we made use of the Bayesian STellar Algorithm BASTA (Silva Aguirre et al. 2015). BASTA uses a Bayesian grid-modelling approach and fits spectroscopic and asteroseismic observables to a large grid of stellar models. We used the grid of stellar models constructed for the *Kepler* LEGACY sample (Lund et al. 2017; Silva Aguirre et al. 2017). The grid is built using GARSTEC evolutionary models (Weiss & Schlattl 2008) with oscillation frequencies computed using ADIPLS (Christensen-Dalsgaard 2008). We used the OPAL05 equation of state (Rogers & Nayfonov 2002), the GS98 solar mixture (Grevesse & Sauval 1998) and OPAL96 (Iglesias & Rogers 1996), and Ferguson et al. (2005) opacities. The inclusion of microscopic diffusion or overshooting does not significantly affect the derived parameters. We fitted the spectroscopically

derived T_{eff} , $\log g$ and $[\text{Fe}/\text{H}]$ and the frequency ratios $r01$, $r10$, and $r02$. We fit frequency ratios (as defined by Roxburgh & Vorontsov 2013) since these are less affected by the asteroseismic surface effect than individual oscillation frequencies, which need corrections to match theoretical frequencies. We report 16, 50, and 84 per cent percentile values from BASTA’s probability distributions. All stellar parameters are listed in Table 3.

As can be seen in this table, there is good agreement between the stellar parameters derived from the two frequency modelling approaches. Both sets of parameters also agree well with the spectroscopic parameters (see Table 1), some of which were used as a prior in the asteroseismic modelling, and the parameters derived from parallax and colour information (see Table 2). The asteroseismic radius and mass have a precision of 1.2 per cent and 3.6 per cent, respectively, which are significantly more precise than the parallax measurements (with a precision of 3.3 and 13 per cent, respectively) and than what can typically be achieved with spectroscopy.

To calculate planetary parameters, we adopt the BASTA stellar parameters, which have been previously used and tested for exoplanet host stars (e.g. Davies et al. 2015; Silva Aguirre et al. 2015; Lund et al. 2017; Silva Aguirre et al. 2017). We show the frequencies of the best BASTA model in Fig. 4, together with the observed frequencies.

3.4 Stellar rotation and inclination

3.4.1 Asteroseismic analysis

As part of the Bayesian frequency determination (Lund et al. 2017) described above, we also modelled the splitting of oscillation frequencies under the influence of rotation (Gizon & Solanki 2003; Ballot, García & Lambert 2006). In some cases, the rotational splitting can provide both the stellar rotation rate and its inclination, leading to a constraint on the obliquity of stars that host transiting planets (see e.g. Chaplin et al. 2013; Lund et al. 2014; Van Eylen et al. 2014; Campante et al. 2016).

Specifically, we modelled the projected splitting ($\nu_s \sin i$, with ν_s the observed frequency splitting and i the stellar inclination) using prior constraints based on the previously determined stellar radius and the spectroscopic $v \sin i$ value. We also tried modelling the splitting without these prior constraints. In both cases the overall result for the inclination is the same, but the best constraint is achieved when using a prior on $v \sin i$ and stellar radius, which corresponds

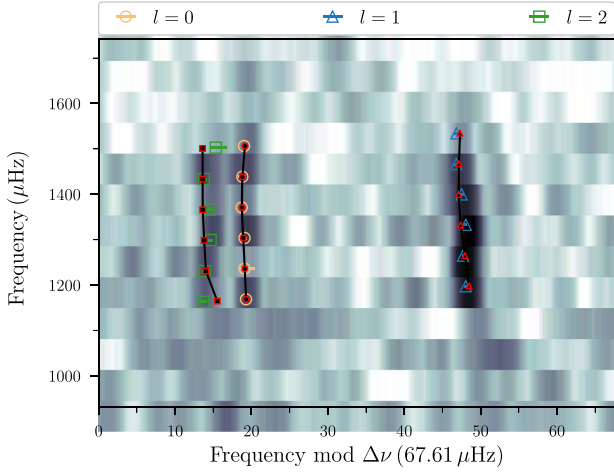


Figure 4. Echelle diagram of HD 89345, showing the observed power as a function of frequency and frequency modulus the large frequency separation. The determined frequencies are shown in different colours and listed in Table A2, and the best model frequencies from BASTA are overplotted with red symbols connected by black lines.

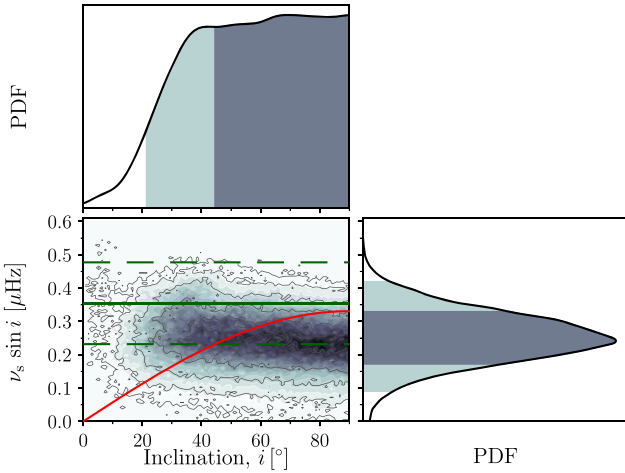


Figure 5. Posterior distribution of the stellar inclination versus the projected rotational splitting of the oscillation frequencies. The splitting of the frequencies is related to $\nu \sin i$ and subject to a Gaussian prior based on the measured projected rotational velocity $\nu \sin i$ and stellar radius (green lines in plot), while the relative amplitudes of the split frequencies provide information about the stellar inclination (see Section 3.4). The red line indicates the projected splitting corresponding to a rotation period of 35 d, as found from analysis of the light curve. In dark blue and light blue, the 68 percent and 95 percent highest probability density intervals are indicated, respectively.

to a prior on the projected rotational splitting of $0.35 \pm 0.13 \mu \text{ Hz}$ [$\nu \sin i = (\nu \sin i)/2\pi R$], and further placing a uniform prior on the cosine of the stellar inclination. As shown in Fig. 5 the inclination is consistent with an aligned orbit, i.e. $i = 90^\circ$, and can at the 1σ limit only be constrained to a lower value of $i \geq 44^\circ$.

The uncertainty is caused by the relatively short duration of K2 photometry. Seismic analysis done with *CoRoT* (Baglin et al. 2006) have placed a limit in the minimum length necessary to have reliable measurements of the inclination angle in G- and K-type stars at about 100 continuous days (e.g. Gizon et al. 2013; Mathur et al. 2013). Using *Kepler*, precise inclination measurements have been measured using several years of observations for many stars, includ-

ing some stars hosting transiting planets (e.g. Chaplin et al. 2013; Huber et al. 2013a; Van Eylen et al. 2014; Campante et al. 2016). We also inspected the K2 light curve for signatures of surface rotation following the methods described in García et al. (2014b). A signal was detected at around 35 d, but due to the short timespan of the observations (≈ 80 d) it is difficult to confirm that this periodicity is indeed the rotation period of the star. We note, however, that a rotation period of 35 d is consistent with the estimated $\nu \sin i$ from spectroscopy and with the estimated projected splitting of $\sim 0.25 \pm 0.1 \mu \text{ Hz}$ at a stellar inclination above the 1σ lower limit (see Fig. 5).

3.4.2 Rossiter–McLaughlin observations

Using in-transit spectroscopic observations (see Section 2.3), we modelled the Rossiter–McLaughlin (RM Rossiter 1924; McLaughlin 1924) effect following the approach of Albrecht et al. (2012) and using the code of Hirano et al. (2011) assuming solid body rotation of the stellar photosphere.

Besides λ , the following model parameters were fitted: $\nu \sin i$, the limb darkening parameters, u_1 and u_2 , the planet-to-star radius ratio, R_p/R_* , the time of mid-transit, t_c , the scaled orbital distance, a/R_* , the RV semi-amplitude of the star, K_* , the systemic velocity of HARPS, γ_{HARPS} , as well as the orbital inclination i , and parameters representing the microturbulence β and macroturbulence ζ . The results from the joint planet modelling (see Section 4 and Table 4) were used as priors on all parameters except for λ , $\nu \sin i$ and γ_{HARPS} . The analysis was done for fixed values of P , e , and ω , since these have minimal influence of the shape of the RM signal. We solved for the best-fitting solution for the parameters and their posterior distribution using an MCMC analysis with EMCEE (Foreman-Mackey et al. 2013). We initialized 120 walkers in the vicinity of the best-fitting solution. We ran the walkers for 1500 steps and discarded the first 800 steps as the burn-in phase.

As can be seen in Fig. 6, the data show no clear RM signal. We find $\nu \sin i = 1.4^{+1.1}_{-0.8} \text{ km s}^{-1}$, which is consistent with the value derived from spectroscopic analysis (see Section 3.1). We further find $\lambda = 2^{+54}_{-30} \text{ deg}$, consistent with alignment, but also with a broad range of obliquities, making it difficult to make conclusive statements about the stellar obliquity.

We caution the reader against overinterpreting this result. As discussed by Albrecht et al. (2011) and Triaud et al. (2017), low SNR detections of the RM effect can lead to spuriously significant results for the projected obliquity. The apparently statistically significant result for λ is based on RV data which appear to have not a significantly higher deviation from the orbital solution – without the modelling of the RM effect – than the out of transit data (see Fig. 6). If a clear detection of the RM effect was made, this would be the case. However, a transit has occurred so two additional free parameters ($\nu \sin i$ and λ) are fitted for, but the RM measurement could be the result of a particular realization of measurement noise. Modelling the data with a systemic velocity (γ) and the orbital velocity (K_*) does in effect apply a high pass filter. The functional forms of the RM effect for 90 and -90 deg orbits have a lower frequency than prograde and retrograde orbits, potentially leading to a spurious result in λ .³ Furthermore, the RM amplitude for projected obliquities near 90 and -90 deg is larger than for 0 and 180 deg

³We note that if the system would have a low impact parameter (which is not the case here) then the RM signal could be suppressed by having polar orbits ($|\lambda| \approx 90 \text{ deg}$) and potential biases for a low-SNR RM measurement would differ.

Table 4. System parameters of HD 89345 (K2-234; EPIC 248777106).

Basic properties		
2MASS ID	10 184 106 + 1007 445	
Right ascension	10 18 41.06	
Declination	+10 07 44.50	
Magnitude (<i>Kepler</i>)	9.204	
Magnitude (<i>V</i>)	9.30	
Magnitude (<i>J</i>)	7.98	
Adopted stellar parameters		
Effective temperature, T_{eff} (K)	5499 ± 73	
Stellar luminosity, $L(L_{\odot})$	$2.27^{+0.21}_{-0.14}$	
Surface gravity, $\log g$ (cgs)	$4.044^{+0.006}_{-0.004}$	
Metallicity, [Fe/H]	0.45 ± 0.04	
Projected rotation speed, $v \sin i$ (km s $^{-1}$)	2.60 ± 0.50	
Stellar mass, M_{\star} (M_{\odot})	$1.120^{+0.040}_{-0.010}$	
Stellar radius, R_{\star} (R_{\odot})	$1.657^{+0.02}_{-0.004}$	
Stellar density, ρ_{\star} (g cm $^{-3}$)	0.343 ± 0.002	
Age (Gyr)	$9.4^{+0.4}_{-1.3}$	
Parameters from RV and transit fit	Circular fit	Eccentric fit (adopted)
Orbital period, P (d)	$11.814\,33 \pm 0.000\,96$	$11.813\,99 \pm 0.000\,86$
Time of conjunction, t_c (BJD−2454833)	$3080.803\,25 \pm 0.000\,66$	$3080.803\,16 \pm 0.000\,62$
Orbital eccentricity, e	0 (fixed)	0.203 ± 0.031
Argument of pericenter, ω ($^{\circ}$)	−	-14.9 ± 20
Stellar radial-velocity amplitude, K_{\star} (m s $^{-1}$)	7.9 ± 1.0	9.49 ± 0.84
Scaled semimajor axis, a/R_{\star}	13.628 ± 0.026	13.625 ± 0.027
Fractional planetary radius, R_p/R_{\star}	$0.038\,40 \pm 0.000\,25$	$0.037\,79 \pm 0.00\,062$
Impact parameter, b	0.5818 ± 0.0084	0.489 ± 0.064
Limb darkening parameter, u_1	0.47 ± 0.10	0.48 ± 0.10
Limb darkening parameter, u_2	0.17 ± 0.14	0.16 ± 0.13
Flux white noise σ	$0.000\,134 \pm 0.000\,023$	$0.000\,134 \pm 0.000\,024$
Covariance amplitude h	$0.000\,0839 \pm 0.000\,0058$	$0.000\,0836 \pm 0.000\,0052$
Covariance time-scale τ (d)	$0.004\,72 \pm 0.000\,80$	$0.004\,85 \pm 0.000\,79$
Stellar jitter term FIES, σ_{FIES} (m s $^{-1}$)	<3.2	<2.5
Stellar jitter term HARPS-N, $\sigma_{\text{HARPS-N}}$ (m s $^{-1}$)	<6.8	<6.3
Stellar jitter term HARPS, σ_{HARPS} (m s $^{-1}$)	<3.2	<2.8
Systemic velocity FIES, γ_{FIES} (m s $^{-1}$)	-2.45 ± 0.91	-2.62 ± 0.97
Systemic velocity HARPS-N, $\gamma_{\text{HARPS-N}}$ (m s $^{-1}$)	2347.4 ± 1.4	2347.5 ± 1.0
Systemic velocity HARPS, γ_{HARPS} (m s $^{-1}$)	2354.5 ± 0.9	2354.2 ± 0.43
Planetary mass, M_p (M_{\oplus})	30.4 ± 3.9	35.7 ± 3.3
Planetary radius, R_p (R_{\oplus})	6.967 ± 0.096	6.86 ± 0.14
Planetary density, ρ_p (g cm $^{-3}$)	0.494 ± 0.067	0.609 ± 0.067
Semimajor axis, a (au)	0.1050 ± 0.0013	0.1050 ± 0.0013
Equilibrium temperature, T_{eq} (K)	1053 ± 14	1053 ± 14

orbits. This is because the maximum RV amplitude of the stellar photosphere, which is covered by the transiting planet, and the lowest level of stellar limb darkening, occur during the same phase for the latter case, but not for the former case (see Albrecht et al. 2013 for details). Taking all this together, we conclude that additional measurements are needed to securely measure the projected obliquity in this system.

4 ORBITAL AND PLANETARY PARAMETERS

4.1 Transit model

To model the transit light curve, we used the PYTHON package BATMAN (Kreidberg 2015). We isolated each transit with a 10 h window around the time of mid-transit. The transit model contains the following parameters: the orbital period P_{orb} , the mid-transit time t_c , the planet-to-star radius ratio R/R_{\star} , the scaled orbital distance

a/R_{\star} , and the impact parameter $b \equiv a \cos i/R_{\star}$, and we adopted the quadratic limb-darkening profile, with parameters u_1 and u_2 .

4.2 Gaussian process model

Evolved stars such as HD 89345 often show correlated flux variations on the time-scales of minutes to hours due to the combination of granulation and pulsation. If unaccounted for, the correlated noise will bias the estimation of transit parameters (Carter & Winn 2009). To model the correlated flux variation, we employed a Gaussian Process regression which is often used to model stellar variability seen in radial-velocity variation of planet host stars (e.g. Haywood et al. 2014; Dai et al. 2017). Here, we adopted a square exponential kernel similar to Grunblatt et al. (2016)

$$C_{i,j} = h^2 \exp \left[-\frac{(t_i - t_j)^2}{2\tau^2} \right] + \sigma^2 \delta_{i,j} \quad (1)$$

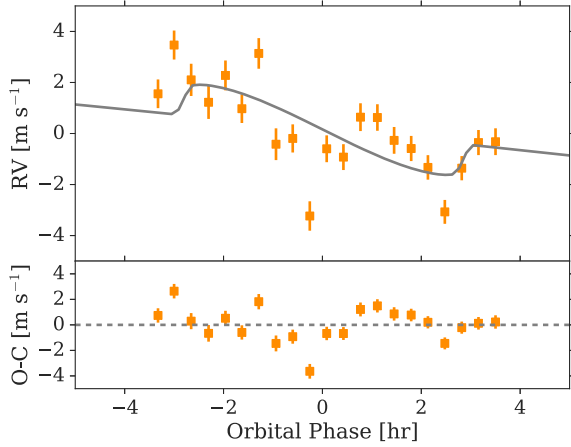


Figure 6. In-transit RV observations measured on the night of 2018 February 23/24 using HARPS. The top panel shows the observations and the best-fitting model of the Rossiter–McLaughlin effect are plotted, as described in Section 3.4.2, and the bottom panel shows the residuals.

where $C_{i,j}$ are the elements of the covariance matrix, $\delta_{i,j}$ is the Kronecker delta function, h is the amplitude of the covariance, t_i is the time of i th flux observation, τ is the correlation time-scale, and σ is the white noise component. The set of parameters h , τ , and σ are known as the hyperparameters of the kernel.

With the above covariance matrix, our likelihood function takes the following form:

$$\log \mathcal{L} = -\frac{N}{2} \log 2\pi - \frac{1}{2} \log |\mathbf{C}| - \frac{1}{2} \mathbf{r}^T \mathbf{C}^{-1} \mathbf{r} \quad (2)$$

where \mathcal{L} is the likelihood, N is the number of flux measurements, \mathbf{C} is the covariance matrix, and \mathbf{r} is the residual vector i.e. the observed flux variation minus the transit model from BATMAN as described in the previous section.

4.3 Radial-velocity model

The final component of our joint analysis is a Keplerian model for the measured radial-velocity variations of the host star. For a circular orbit, the three parameters of the Keplerian models are the RV semi-amplitude K , the orbital period P_{orb} , and time of conjunction t_c . We also experimented with an eccentric orbit, which introduces two additional parameters: the eccentricity e and the argument of periastron ω . For unbiased sampling, we transformed these parameters to $\sqrt{e} \cos \omega$ and $\sqrt{e} \sin \omega$ (Lucy & Sweeney 1971; Anderson et al. 2011). For each of the spectrographs we used, we included a systematic offset γ and a jitter σ_{jit} parameter which subsumes any additional instrumental and stellar noise.

The likelihood function for the radial-velocity measurement takes the following form:

$$\mathcal{L} = \prod_i \left(\frac{1}{\sqrt{2\pi(\sigma_i^2 + \sigma_{\text{jit}}(t_i)^2)}} \exp \left[-\frac{[RV(t_i) - \mathcal{M}(t_i) - \gamma(t_i)]^2}{2(\sigma_i^2 + \sigma_{\text{jit}}(t_i)^2)} \right] \right), \quad (3)$$

where $RV(t_i)$ is the measured radial velocity at time t_i ; $\mathcal{M}(t_i)$ is the Keplerian model at time t_i ; σ_i is the internal measurement uncertainty; $\sigma_{\text{jit}}(t_i)$ and $\gamma(t_i)$ are the jitter and offset parameters depending on which instrument was used to obtain the measurement $RV(t_i)$.

To avoid confusion with the Rossiter–McLaughlin effect, we exclude RV points taken within 8 h window around the predicted

mid-transit time from this analysis. These data points are modelled separately (see Section 3.4.2).

4.4 Joint analysis

To summarize, the free parameters in our joint analysis include the orbital period P_{orb} , the mid-transit time t_c , the planet-to-star radius ratio R_p/R_* , the scaled orbital distance a/R_* , the impact parameter $b \equiv a \cos i/R_*$, the limb-darkening profile u_1 and u_2 ; the orbital eccentricity parameters $\sqrt{e} \cos \omega$ and $\sqrt{e} \sin \omega$; the amplitude of the covariance h ; the correlation time-scale τ ; the white noise component of the light-curve σ ; the RV semi-amplitude K ; the systematic offset and jitter for each spectrograph γ , σ_{jit} . We sampled all the scale parameters (P_{orb} , R_p/R_* , a/R_* , h , τ , σ , and σ_{jit}) uniformly in log space, which effectively imposes the Jeffreys prior. We included a prior on the mean stellar density inferred from the asteroseismic analysis $\rho_* = 0.343 \pm 0.002 \text{ g cm}^{-3}$ using equation 30 of Winn (2010). We imposed Gaussian priors on the limb-darkening coefficients u_1 and u_2 using the median values from EXOFAST⁴ (Eastman, Gaudi & Agol 2013) and widths of 0.2. We imposed a uniform prior on the other parameters.

Our final likelihood function is the simple addition of equation (2) and the natural logarithm of equation (3). We first located the best-fitting solution using the Levenberg–Marquardt algorithm implemented in the PYTHON package LMFIT. We show the best-fitting transits, including Gaussian processes, in Fig. 7, the best-fitting folded transit in Fig. 8, and the best radial-velocity model for both the circular and the eccentric case in Fig. 9. To sample the posterior distribution of various parameters, we ran an MCMC analysis with EMCEE (Foreman-Mackey et al. 2013). We initialized 128 walkers in the vicinity of the best-fitting solution. We ran the walkers for 5000 steps and discarded the first 1000 steps as the burn-in phase. We report all parameters in Table 4 using the 16, 50, and 84 per cent percentile cumulative posterior distribution.

4.5 Orbital eccentricity

We find a best-fitting orbital eccentricity of 0.203 ± 0.031 . However, a perfectly circular orbit also provides a reasonable fit to the data, despite the smaller number of parameters. We used the Bayesian Information Criterion (BIC) to check on whether adding the additional two degrees of freedom for an eccentric orbit is justified. We have 5300 flux observations and 46 RV measurements. The circular model contains 15 parameters, while the eccentric model contains 17. We find a difference in BIC values of 19 between the eccentric fit and the circular fit, favouring the eccentric solution.

When the mean stellar density is known from external observations, the transit duration contains information about the orbital eccentricity (e.g. Ford, Quinn & Veras 2008). We investigated the resulting constraint on the eccentricity by fitting the transit data alone (not taking into account the RV observations). Following the procedure described by Van Eylen & Albrecht (2015), we found $e = 0.10^{+0.07}_{-0.10}$, with an uncertainty that is strongly correlated with that of the impact parameter. Lower impact parameters correspond to higher eccentricity. Alternatively, this measurement shows that the stellar density that can be derived from the transit photometry is consistent with that of the asteroseismic analysis, for near-circular orbits. We note that this solution did not make use of the Gaussian processes described above, but nevertheless resulted in consistent

⁴astroutils.astronomy.ohio-state.edu/exofast/limbdark.shtml.

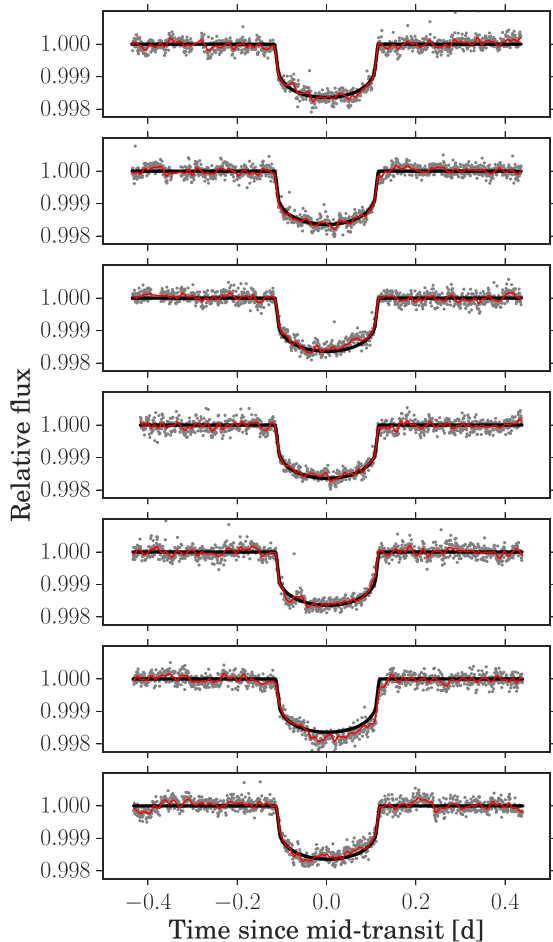


Figure 7. The transits observed with K2 are shown in grey. Overplotted is the best transit model (black) and the best transit model including Gaussian processes (red), for the eccentric fitting case (see Section 4.5).

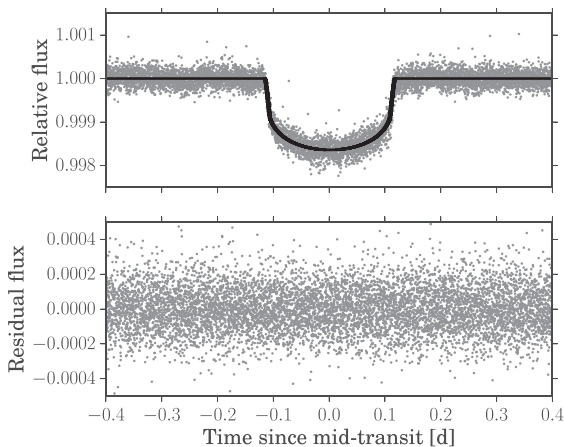


Figure 8. Combined K2 transits (grey) together with the best-fitting model (black), not taking into account the Gaussian processes. The bottom panel shows the residuals.

planetary parameters. This solution is consistent with both a circular orbit and with the eccentric fit solution to the combined transit and RV data, at the 95 per cent confidence level.

In Table 4, we list all parameters for both the circular and the eccentric solution. However, as the eccentric solution is favoured by the data, we adopt these values in the discussion below.

5 DISCUSSION

5.1 Stellar properties

HD 89345 is at an interesting phase of its evolution. The star has just evolved off the main sequence, as can be seen in the Hertzsprung–Russell diagram (see Fig. 10). From the best-fitting model, it appears to be at the edge of the turn-off point, being a hydrogen shell-burning star with a non-degenerate helium core of 0.06 stellar masses. This explains why no mixed modes were detected in the observed frequency range. In most previous cases of solar-like oscillators for which the individual frequencies were studied using data from *CoRoT* (Baglin et al. 2006) or *Kepler* (Borucki et al. 2010), the star was either found to be firmly on the main sequence, or firmly on the subgiant branch (e.g. Mathur et al. 2012; Silva Aguirre et al. 2015; Creevey et al. 2017). Fig. 10 shows the stars with asteroseismic analysis of individual oscillation frequencies, for planet-host stars and stars not known to have planets, from the *Kepler* mission. We can see that our target is in a sparsely populated region of this diagram.

Previously, several asteroseismic studies have investigated evolved planet hosting stars, such as subgiant and giant stars, with *Kepler* (e.g. Huber et al. 2013a,b; Silva Aguirre et al. 2015; Davies et al. 2016), as well as with K2 (e.g. Grunblatt et al. 2016; North et al. 2017). The system investigated here is less evolved, and has only just left the main sequence (see Fig. 10). As a result, the oscillation frequencies cannot be detected with the standard long-cadence (30 min integration) K2 observations. Here, the availability of short-cadence observations enabled the asteroseismic measurement.

The depth of the convective zone is 32 per cent of the stellar radius, and the depth of the helium second ionization zone is 3 per cent of the stellar radius. These values are obtained as the best-fitting parameters from the modelling, as *p*-mode oscillations of subgiant stars are very sensitive to the location of these layers (see e.g. Grunhagel et al. 2017). Both zones are a bit deeper in this star than they are in the Sun. Locating the position of the base of the convective zone is interesting in order to better understand the mechanism of the stellar dynamo, while the helium second ionization zone provides insights in the process of chemical enrichment in stars.

5.2 Planet properties

HD 89345b is a sub-Saturn planet, with a radius of $6.86 \pm 0.14 R_{\oplus}$. In the Solar system, no planets exist with a size between Uranus ($4 R_{\oplus}$) and Saturn ($9.45 R_{\oplus}$). Sub-Saturn planets span a wide range of masses, spanning from 6 to 60 M_{\oplus} , independent of their size (Petigura et al. 2017). Although similar to Jovian planets in that they have a large envelope of hydrogen and helium gas, sub-Saturns have much lower masses. This suggests that sub-Saturns did not undergo runaway gas accretion. Alternative scenarios have been proposed, such as accretion within a depleted gas disc (Lee & Chiang 2015).

HD 89345b joins a list of 24 sub-Saturns with a mean density measured to better than 50 per cent (see Petigura et al. 2017; table 7). In these systems, Petigura et al. (2017) find that higher mass

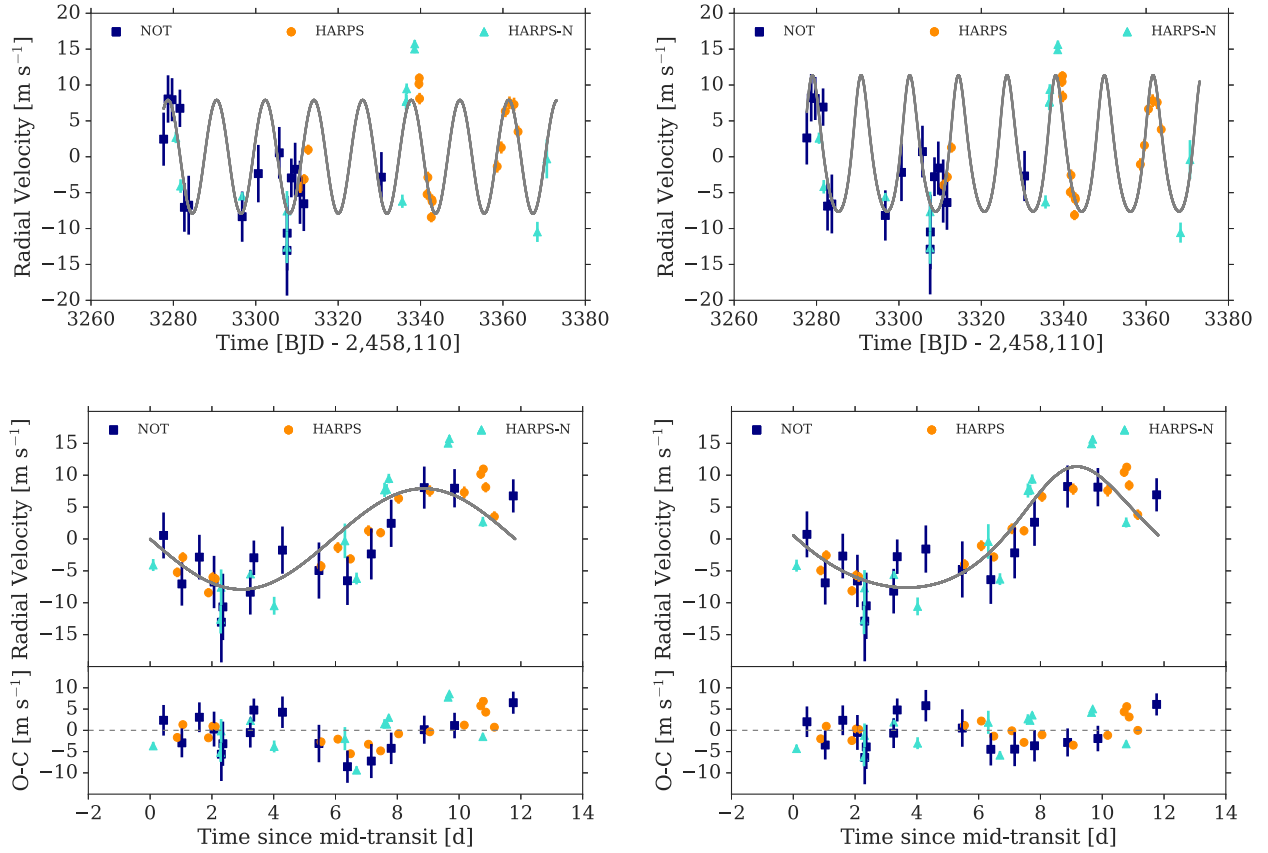


Figure 9. Radial-velocity measurements from FIES, HARPS, and HARPS-N are indicated in different colours and symbols. RV points within 8 h of the transit window are excluded. The top plots show the observations as a function of time. The bottom plots show the observation as a function of phase and include the residuals (observed minus calculated, $O - C$). In the plots on the left, the best circular model is plotted. In the plots on the right, the best eccentric model is plotted. The observations are provided in Table A1 and the best values for the models are given in Table 4.

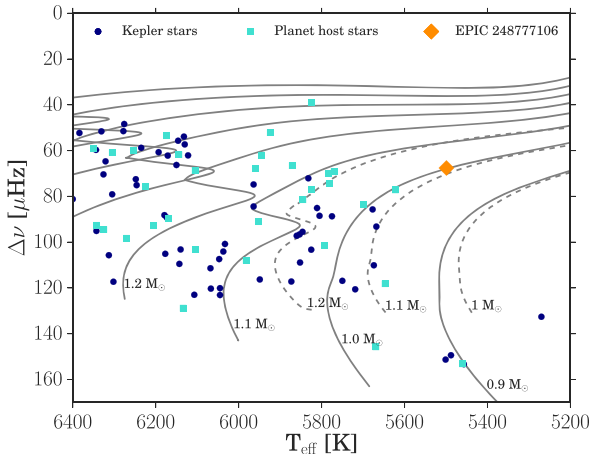


Figure 10. Modified HR diagram, which depicts the large frequency separation and the effective temperature. In light blue squares, we show solar-like oscillating stars for which the individual frequencies were modeled by Lund et al. (2017). The dark blue circles are the planet-host stars, taken from Davies et al. (2016) with a detailed modelling performed by Silva Aguirre et al. (2015). The orange square shows the star analysed in this work. Evolution tracks (using the ASTEC models) are shown for a range of masses at solar composition ($Z_{\odot} = 0.0246$) in grey solid lines and for $\text{Fe}/\text{H} = 0.45$ dex (GARSTEC models) in dashed grey lines.

planets are associated with a higher stellar metallicity, a low-planet multiplicity, and a non-zero orbital eccentricity. HD 89345b has a relatively high mass, orbits a star with a relatively high metallicity, is the only detected planet in the system, and appears to have an eccentric orbit. It therefore fits all of these expectations, as shown in Fig. 11.

Here, we have adopted the planet’s eccentric orbital solution. We estimate the time-scale of circularization following Goldreich & Soter (1966) and using a modified tidal quality factor of $Q' = 10^5$ as suggested by Petigura et al. (2017), and find a circularization time-scale of 18 Gyr, suggesting that if the orbit was eccentric early in its formation, it could still be eccentric today. However, recent high-precision astrometric data obtained with the *CASSINI* space mission suggest a stronger value for the current tidal dissipation in Saturn, with a modified tidal quality factor $Q' \approx 9434$ (Lainey et al. 2017). Assuming such a value, which can be explained by different ab-initio models of tidal dissipation both in the potential rocky/icy core of the planet (Remus et al. 2012; Lainey et al. 2017) or in its fluid envelope (Ogilvie & Lin 2004; Guenel, Mathis & Remus 2014; Fuller, Luan & Quataert 2016), the circularization time-scale will be shorter, i.e. 1.69 Gyr, a value that is also compatible with the age of the host star. Therefore, the apparent eccentric orbit suggests a weaker dissipation in warm Saturns than in Saturn, which is similar to the weaker dissipation in hot Jupiters than in Jupiter, as has been previously suggested (Ogilvie 2014 and references therein).

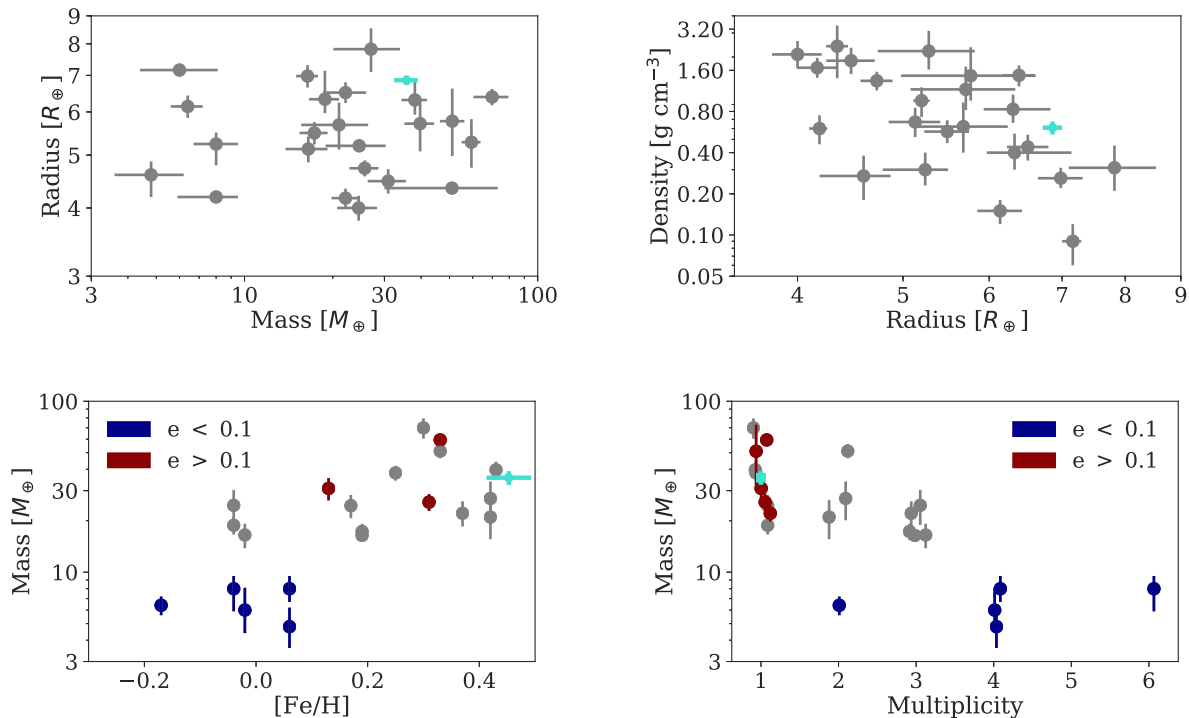


Figure 11. The properties of sub-Saturns as listed in Petigura et al. (2017) are listed in grey. In the bottom plot, we use red and blue symbols when the eccentricity is clearly established (again following Petigura et al. 2017), for eccentric and circular orbits, respectively. HD 89345b is shown in a light blue square. As a relatively high-mass sub-Saturn planet, HD 89345b fits the pattern as a single detected planet with a significant eccentricity orbiting a metal-rich star. For the multiplicity, the values are slightly offset for clarity.

The flux of radiation that the planet receives from the star is roughly 150 times the flux the Earth receives from the Sun. Thus the planet is heavily irradiated, but not quite at the level at which evidence of photoevaporation is seen (Fulton et al. 2017; Van Eylen et al. 2017).

5.3 Future work

We investigated the rotational splitting of the stellar oscillations, which have the potential to reveal the stellar inclination angle. However, the posterior distribution of this analysis is consistent with a wide range of stellar inclination angles. Similarly, Rossiter–McLaughlin observations cannot reliably constrain the stellar obliquity. Future such measurements, although challenging for shallow transits, may lead to a clearer detection of the Rossiter–McLaughlin effect, owing to the brightness of the host star. The medium-level impact parameter further facilitates such studies.

Due to its low density, HD 89345b may be a target for atmospheric characterization. However, given the large stellar radius, the expected transmission signal per scale height (H) of the planetary atmosphere, assuming an H_2/He dominated atmosphere with $\mu = 2.3$, is only 48 parts per million (ppm). Under the same assumption, and also assuming that its atmosphere exhibits pure Rayleigh scattering, the transit depth difference between g' and z' bands would be about 140 ppm (see e.g. Madhusudhan et al. 2016; for details). If the mean molecular weight were closer to that of Neptune rather than Jupiter, the transmission signal would be even smaller. Given these numbers, atmospheric characterization would likely be out of reach for most instruments, except perhaps for the *James Webb Space Telescope* (Gardner et al. 2006).

Asteroseismology of planet host stars has been a fruitful endeavor with the *Kepler* mission, but has so far been limited to evolved stars for K2. This is the least evolved planet host star for which asteroseismology has been possible with only 80 d of K2 observations.

The detection of individual stellar oscillation modes, and even moderate constraints on the rotational splittings, with 80 d of photometry, is encouraging for asteroseismic detection with the upcoming *TESS* mission (Ricker et al. 2014), which will provide one month of observations for the most bright stars in the sky, as well as longer photometric time series for certain regions of the sky.

ACKNOWLEDGEMENTS

We gratefully acknowledge many helpful suggestions by the anonymous referee. Based on observations made with a) the Nordic Optical Telescope, operated by the Nordic Optical Telescope Scientific Association at the Observatorio del Roque de los Muchachos; b) the ESO-3.6m telescope at La Silla Observatory under programme ID 0100.C-0808; c) the Italian Telescopio Nazionale Galileo operated on the island of La Palma by the Fundación Galileo Galilei of the Istituto Nazionale di Astrofisica. NESSI was funded by the NASA Exoplanet Exploration Program and the NASA Ames Research Center. NESSI was built at the Ames Research Center by Steve B. Howell, Nic Scott, Elliott P. Horch, and Emmett Quigley. This project has received funding from the European Union’s Horizon 2020 research and innovation programme under grant agreement No 730890. This material reflects only the authors views and the Commission is not liable for any use that may be made of the information contained therein. DG gratefully acknowledges the financial support of the *Programma Giovani Ricercatori – Rita Levi Montalcini – Rientro dei Cervelli* (2012) awarded by the Italian

Ministry of Education, Universities and Research (MIUR). SaM would like to acknowledge support from the Ramon y Cajal fellowship number RYC-2015-17697. AJ, MH, and SA acknowledge support by the Danish Council for Independent Research, through a DFF Sapere Aude Starting Grant nr. 4181-00487B. SzCs, APH, MP, and HR acknowledge the support of the DFG priority program SPP 1992 Exploring the Diversity of Extrasolar Planets (grants HA 3279/12-1, PA 525/18-1, PA 525/19-1 and PA 525/20-1, RA 714/14-1) HD, CR, and FPH acknowledge the financial support from MINECO under grants ESP2015-65712-C5-4-R and AYA2016-76378-P. This paper has made use of the IAC Supercomputing facility HTCondor (<http://research.cs.wisc.edu/htcondor/>), partly financed by the Ministry of Economy and Competitiveness with FEDER funds, code IACA13-3E-2493. MF and CMP gratefully acknowledge the support of the Swedish National Space Board. RAG and StM thanks the support of the CNES PLATO grant. PGB is a postdoctoral fellow in the MINECO-programme 'Juan de la Cierva Incorporación' (IJC1-2015-26034). StM acknowledges support from ERC through SPIRE grant (647383) and from ISSI through the ENCELADE 2.0 team. VSA acknowledges support from VILLUM FONDEN (research grant 10118). MNL acknowledges support from the ESA-PRODEX programme. Funding for the Stellar Astrophysics Centre is provided by The Danish National Research Foundation (Grant agreement no.: DNR106) This work has made use of data from the European Space Agency (ESA) mission *Gaia* (<https://www.cosmos.esa.int/gaia>), processed by the *Gaia* Data Processing and Analysis Consortium (DPAC, <https://www.cosmos.esa.int/web/gaia/dpac/consortium>). Funding for the DPAC has been provided by national institutions, in particular the institutions participating in the *Gaia* Multilateral Agreement. This research was made with the use of NASA's Astrophysics Data System and the NASA Exoplanet Archive, which is operated by the California Institute of Technology, under contract with the National Aeronautics and Space Administration under the Exoplanet Exploration Program.

REFERENCES

- Albrecht S. et al., 2011, *ApJ*, 738, 50
 Albrecht S. et al., 2012, *ApJ*, 757, 18
 Albrecht S., Winn J. N., Marcy G. W., Howard A. W., Isaacson H., Johnson J. A., 2013, *ApJ*, 771, 11
 Anderson D. R. et al., 2011, *ApJ*, 726, L19
 Baglin A. et al., 2006, in 36th COSPAR Scientific Assembly, held in Beijing, 2006 July 16-23, Meeting Abstract #3749
 Ballot J., García R. A., Lambert P., 2006, *MNRAS*, 369, 1281
 Borucki W. J. et al., 2010, *Science*, 327, 977
 Brown T. M., Latham D. W., Everett M. E., Esquerdo G. A., 2011, *AJ*, 142, 112
 Bruntt H. et al., 2010, *MNRAS*, 405, 1907
 Campante T. L. et al., 2016, *ApJ*, 819, 85
 Carter J. A., Winn J. N., 2009, *ApJ*, 704, 51
 Casagrande L., VandenBerg D. A., 2014, *MNRAS*, 444, 392
 Chaplin W. J. et al., 2013, *ApJ*, 766, 101
 Christensen-Dalsgaard J., 2008, *Ap&SS*, 316, 113
 Cosentino R. et al., 2012, in Proc. SPIE Conf. Ser. Vol. 8446, Ground-based and Airborne Instrumentation for Astronomy IV. SPIE, Bellingham. p. 84461V
 Creevey O. L. et al., 2017, *A&A*, 601, A67
 Cutri R. M. et al., 2003, The IRSA 2MASS All-Sky Point Source Catalog, NASA/IPAC Infrared Science Archive. Available at <http://irsa.ipac.caltech.edu/applications/Gator/>
 Dai F. et al., 2017, *AJ*, 154, 226
 Davies G. R. et al., 2015, *MNRAS*, 446, 2959
 Davies G. R. et al., 2016, *MNRAS*, 456, 2183
 Doyle A. P., Davies G. R., Smalley B., Chaplin W. J., Elsworth Y., 2014, *MNRAS*, 444, 3592
 Eastman J., Gaudi B. S., Agol E., 2013, *PASP*, 125, 83
 Ferguson J. W., Alexander D. R., Allard F., Barman T., Bodnarik J. G., Hauschildt P. H., Heffner-Wong A., Tamanai A., 2005, *ApJ*, 623, 585
 Ford E. B., Quinn S. N., Veras D., 2008, *ApJ*, 678, 1407
 Foreman-Mackey D., Hogg D. W., Lang D., Goodman J., 2013, *PASP*, 125, 306
 Frandsen S., Lindberg B., 1999, in Karttunen H., Pirola V., eds, Astrophysics with the NOT. p. 71
 Fridlund M. et al., 2017, *A&A*, 604, A16
 Fuhrmann K., Axer M., Gehren T., 1993, *A&A*, 271, 451
 Fuhrmann K., Axer M., Gehren T., 1994, *A&A*, 285, 585
 Fuller J., Luan J., Quataert E., 2016, *MNRAS*, 458, 3867
 Fulton B. J. et al., 2017, *AJ*, 154, 109
 Gaia Collaboration Brown A. G. A., Vallenari A., Prusti T., de Bruijne J. H. J., Babusiaux C., Bailer-Jones C. A. L., 2018, preprint ([arXiv:1804.09365](https://arxiv.org/abs/1804.09365))
 Gaia Collaboration, 2016a, *A&A*, 595, A1
 Gaia Collaboration, 2016b, *A&A*, 595, A2
 Gandolfi D. et al., 2013, *A&A*, 557, A74
 Gandolfi D. et al., 2017, *AJ*, 154, 123
 García R. A. et al., 2011, *MNRAS*, 414, L6
 García R. A. et al., 2014a, *A&A*, 568, A10
 García R. A. et al., 2014b, *A&A*, 572, A34
 Gardner J. P. et al., 2006, *Space Sci. Rev.*, 123, 485
 Gizon L., Solanki S. K., 2003, *ApJ*, 589, 1009
 Gizon L. et al., 2013, *Proc. Natl. Acad. Sci.*, 110, 13267
 Goldreich P., Soter S., 1966, *Icarus*, 5, 375
 Gray D. F., 1984, *ApJ*, 281, 719
 Green G. M. et al., 2015, *ApJ*, 810, 25
 Grevesse N., Sauval A. J., 1998, *Space Sci. Rev.*, 85, 161
 Grunblatt S. K. et al., 2016, *AJ*, 152, 185
 Grundahl F. et al., 2017, *ApJ*, 836, 142
 Guenel M., Mathis S., Remus F., 2014, *A&A*, 566, L9
 Haywood R. D. et al., 2014, *MNRAS*, 443, 2517
 Herwig F., 2000, *A&A*, 360, 952
 Hirano T., Suto Y., Winn J. N., Taruya A., Narita N., Albrecht S., Sato B., 2011, *ApJ*, 742, 69
 Howell S. B., Everett M. E., Sherry W., Horch E., Ciardi D. R., 2011, *AJ*, 142, 19
 Howell S. B. et al., 2014, *PASP*, 126, 398
 Huber D. et al., 2013a, *Science*, 342, 331
 Huber D. et al., 2013b, *ApJ*, 767, 127
 Høg E. et al., 2000, *A&A*, 355, L27
 Iglesias C. A., Rogers F. J., 1996, *ApJ*, 464, 943
 Kjeldsen H., Bedding T. R., 1995, *A&A*, 293, 87
 Kovács G., Zucker S., Mazeh T., 2002, *A&A*, 391, 369
 Kreidberg L., 2015, *PASP*, 127, 1161
 Kuerster M., Schmitt J. H. M. M., Cutispoto G., Dennerl K., 1997, *A&A*, 320, 831
 Kurucz R. L., 2013, ATLAS12: Opacity sampling model atmosphere program, Astrophysics Source Code Library, record ascl:1303.024
 Lainey V. et al., 2017, *Icarus*, 281, 286
 Lee E. J., Chiang E., 2015, *ApJ*, 811, 41
 Lucy L. B., Sweeney M. A., 1971, *AJ*, 76, 544
 Lund M. N. et al., 2014, *A&A*, 570, A54
 Lund M. N. et al., 2016, *PASP*, 128, 124204
 Lund M. N. et al., 2017, *ApJ*, 835, 172
 Luri X. et al., 2018, preprint ([arXiv:1804.09376](https://arxiv.org/abs/1804.09376))
 Madhusudhan N., Agúndez M., Moses J. I., Hu Y., 2016, *Space Sci. Rev.*, 205, 285
 Mathur S. et al., 2010, *A&A*, 511, A46
 Mathur S. et al., 2012, *ApJ*, 749, 152
 Mathur S., García R. A., Morgenthaler A., Salabert D., Petit P., Ballot J., Régulo C., Catala C., 2013, *A&A*, 550, A32
 Mayor M. et al., 2003, *Messenger*, 114, 20

McLaughlin D. B., 1924, *ApJ*, 60
 North T. S. H. et al., 2017, *MNRAS*, 472, 1866
 Ogilvie G. I., 2014, *ARA&A*, 52, 171
 Ogilvie G. I., Lin D. N. C., 2004, *ApJ*, 610, 477
 Paxton B., Bildsten L., Dotter A., Herwig F., Lesaffre P., Timmes F., 2011, *ApJS*, 192, 3
 Pérez Hernández F., García R. A., Corsaro E., Triana S. A., De Ridder J., 2016, *A&A*, 591, A99
 Petigura E. A. et al., 2017, *AJ*, 153, 142
 Pietrinferni A., Cassisi S., Salaris M., Castelli F., 2004, *ApJ*, 612, 168
 Pires S., Mathur S., García R. A., Ballot J., Stello D., Sato K., 2015, *A&A*, 574, A18
 Piskunov N., Valenti J. A., 2017, *A&A*, 597, A16
 Remus F., Mathis S., Zahn J.-P., Lainey V., 2012, *A&A*, 541, A165
 Ricker G. R. et al., 2014, in Oschmann J. M., Clampin M., Fazio G. G., MacEwen H. A., eds, *Proc. SPIE Conf. Ser. Vol. 9143, Space Telescopes and Instrumentation 2014: Optical, Infrared, and Millimeter Wave*. SPIE, Bellingham, p. 914320
 Roca Cortés T., Jiménez A., Pallé P. L. GOLF Team Virgo Team 1999, in Wilson A. et al. eds, *ESA Special Publication Vol. 448, Magnetic Fields and Solar Processes*. ESA, Noordwijk, p. 135
 Rogers F. J., Nayfonov A., 2002, *ApJ*, 576, 1064
 Rossiter R. A., 1924, *ApJ*, 60
 Roxburgh I. W., Vorontsov S. V., 2013, *A&A*, 560, A2
 Sanchis-Ojeda R. et al., 2015, *ApJ*, 812, 112
 Scott N. J., Howell S. B., Horch E. P., 2016, in *Proc. SPIE Conf. Ser. Vol. 9907, Optical and Infrared Interferometry and Imaging V*. p. 99072R
 Silva Aguirre V. et al., 2015, *MNRAS*, 452, 2127
 Silva Aguirre V. et al., 2017, *ApJ*, 835, 173
 Smith A. M. S. et al., 2018, *MNRAS*, 474, 5523
 Telting J. H. et al., 2014, *Astron. Nachr.*, 335, 41
 Triaud A. H. M. J. et al., 2017, *MNRAS*, 467, 1714
 Valenti J. A., Fischer D. A., 2005, *ApJS*, 159, 141
 Valenti J. A., Piskunov N., 1996, *A&AS*, 118, 595
 Van Eylen V., Albrecht S., 2015, *ApJ*, 808, 126
 Van Eylen V. et al., 2014, *ApJ*, 782, 14
 Van Eylen V. et al., 2016a, *AJ*, 152, 143
 Van Eylen V. et al., 2016b, *ApJ*, 820, 56
 Van Eylen V., Agentoft C., Lundkvist M. S., Kjeldsen H., Owen J. E., Fulton B. J., Petigura E., Snellen I., 2017, preprint ([arXiv:1710.05398](https://arxiv.org/abs/1710.05398))
 Vanderburg A., Johnson J. A., 2014, *PASP*, 126, 948
 Weiss A., Schlattl H., 2008, *Ap&SS*, 316, 99
 Winn J. N., 2010, *Exoplanet Transits and Occultations*. Univ. of Arizona Press, Tucson, AZ, p. 55
 Yu L. et al., 2018, preprint ([arXiv:1803.02858](https://arxiv.org/abs/1803.02858))
 Zechmeister M., Kürster M., 2009, *A&A*, 496, 577

APPENDIX A: EXTRA MATERIAL

- ¹*Leiden Observatory, Leiden University, postbus 9513, NL-2300 RA Leiden, the Netherlands*
- ²*Department of Physics and Kavli Institute for Astrophysics and Space Research, Massachusetts Institute of Technology, Cambridge, MA 02139, USA*
- ³*Department of Astrophysical Sciences, Princeton University, 4 Ivy Lane, Princeton, NJ 08544, USA*
- ⁴*Departamento de Astrofísica, Universidad de La Laguna, E-38206 Tenerife, Spain*
- ⁵*Instituto de Astrofísica de Canarias, C/Vía Láctea s/n, La Laguna, E-38205 Tenerife, Spain*
- ⁶*Dipartimento di Fisica, Università degli Studi di Torino, via Pietro Giuria 1, I-10125 Torino, Italy*
- ⁷*Stellar Astrophysics Centre, Department of Physics and Astronomy, Aarhus University, Ny Munkegade 120, DK-8000 Aarhus C, Denmark*
- ⁸*Department of Space, Earth and Environment, Chalmers University of Technology, Onsala Space Observatory, SE-439 92 Onsala, Sweden*
- ⁹*IRFU, CEA, Université Paris-Saclay, F-91191 Gif-sur-Yvette, France*
- ¹⁰*Université Paris Diderot, AIM, Sorbonne Paris Cité, CEA, CNRS, F-91191 Gif-sur-Yvette, France*
- ¹¹*Thüringer Landessternwarte Tautenburg, Sternwarte 5, D-07778 Tautenburg, Germany*
- ¹²*Department of Astronomy, Graduate School of Science, The University of Tokyo, Hongo 7-3-1, Bunkyo-ku, Tokyo 113-0033, Japan*
- ¹³*National Optical Astronomy Observatory, 950 North Cherry Avenue Tucson, AZ 85719, USA*
- ¹⁴*Department of Earth and Planetary Sciences, Tokyo Institute of Technology, 2-12-1 Ookayama, Meguro-ku, Tokyo 152-8551, Japan*
- ¹⁵*Max-Planck-Institut für Astronomie, Königstuhl 17, D-69117 Heidelberg, Germany*
- ¹⁶*School of Physics and Astronomy, University of Birmingham, Edgbaston, Birmingham B15 2TT, UK*
- ¹⁷*Department of Astronomy and McDonald Observatory, University of Texas at Austin, 2515 Speedway, Stop C1400, Austin, TX 78712, USA*
- ¹⁸*Institute of Planetary Research, German Aerospace Center, Rutherfordstrasse 2, D-12489 Berlin, Germany*
- ¹⁹*ZAH-Landessternwarte Heidelberg, Königstuhl 12, D-69117 Heidelberg, Germany*
- ²⁰*Rheinisches Institut für Umweltforschung, Abteilung Planetenforschung an der Universität zu Köln, Aachener Strasse 209, D-50931 Köln, Germany*
- ²¹*National Astronomical Observatory of Japan, NINS, 2-21-1 Osawa, Mitaka, Tokyo 181-8588, Japan*

Table A1. Radial-velocity observations (see Section 2.3 for details). Notes. ¹SNR calculated per pixel at 5500 Å. ² The SNR in the blue part of the spectrum was too low to calculate these \log_{RHK} values.

Time [BJD]	RV [km s ⁻¹]	σ_{RV} [km s ⁻¹]	Ins.	BIS [km s ⁻¹]	FWHM [km s ⁻¹]	\log_{RHK}	$\sigma(\log_{\text{RHK}})$	t_{exp}	SNR ⁽¹⁾
2458110.635193	0.0000	0.0037	FIES	0.0004	12.6730	–	–	1800.0	98.8
2458111.705789	0.0056	0.0033	FIES	0.0001	12.6718	–	–	1800.0	71.2
2458112.686073	0.0055	0.0030	FIES	0.0022	12.6721	–	–	1200.0	97.0
2458114.586884	0.0043	0.0026	FIES	0.0040	12.6676	–	–	2400.0	98.1
2458115.674859	–0.0095	0.0034	FIES	0.0047	12.6412	–	–	1800.0	68.6
2458116.716467	–0.0092	0.0041	FIES	0.0012	12.6529	–	–	1800.0	65.4
2458129.703737	–0.0108	0.0035	FIES	–0.0021	12.6590	–	–	1800.0	73.0
2458133.620112	–0.0048	0.0040	FIES	–0.0042	12.6488	–	–	1800.0	70.7
2458138.710781	–0.0019	0.0036	FIES	–0.0056	12.6181	–	–	1800.0	65.2
2458140.581356	–0.0155	0.0063	FIES	–0.0045	12.6574	–	–	3600.0	39.1
2458140.630614	–0.0131	0.0052	FIES	–0.0036	12.6471	–	–	3600.0	44.3
2458141.633063	–0.0054	0.0027	FIES	0.0136	12.6659	–	–	1800.0	97.1
2458142.559006	–0.0042	0.0037	FIES	0.0000	12.6593	–	–	2700.0	67.7
2458143.739530	–0.0074	0.0044	FIES	–0.0032	12.6387	–	–	3600.0	59.0
2458144.662520	–0.0090	0.0038	FIES	–0.0027	12.6575	–	–	1800.0	68.8
2458163.498602	–0.0053	0.0035	FIES	–0.0016	12.6668	–	–	1800.0	70.5
2458143.808287	2.3502	0.0008	HARPS	0.0018	7.6348	–5.1690	0.0138	1200.0	98.4
2458144.759327	2.3514	0.0007	HARPS	0.0007	7.6311	–5.1684	0.0111	1200.0	109.4
2458145.736594	2.3555	0.0007	HARPS	0.0021	7.6289	–5.1846	0.0116	1500.0	106.9
2458172.606520	2.3646	0.0007	HARPS	0.0016	7.6303	–5.1321	0.0096	1200.0	101.7
2458172.689287	2.3654	0.0006	HARPS	0.0060	7.6271	–5.1589	0.0095	1200.0	116.1
2458172.767539	2.3626	0.0008	HARPS	–0.0033	7.6303	–5.1781	0.0153	900.0	97.2
2458173.566565	2.3594	0.0007	HARPS	0.0026	7.6321	–5.1514	0.0111	1200.0	100.2
2458173.580118	2.3613	0.0008	HARPS	0.0004	7.6283	–5.1327	0.0104	1200.0	98.8
2458173.594505	2.3599	0.0009	HARPS	0.0042	7.6364	–5.1725	0.0137	1200.0	88.3
2458173.609169	2.3590	0.0009	HARPS	0.0057	7.6253	–5.1520	0.0138	1200.0	85.5
2458173.623405	2.3601	0.0008	HARPS	0.0062	7.6299	–5.1486	0.0113	1200.0	95.8
2458173.637236	2.3588	0.0007	HARPS	0.0032	7.6329	–5.1351	0.0102	1200.0	100.5
2458173.651484	2.3609	0.0008	HARPS	0.0022	7.6302	–5.1681	0.0123	1200.0	93.7
2458173.666009	2.3574	0.0008	HARPS	0.0041	7.6284	–5.1393	0.0124	1200.0	90.2
2458173.680106	2.3576	0.0007	HARPS	0.0029	7.6354	–5.1305	0.0104	1200.0	103.4
2458173.694493	2.3546	0.0008	HARPS	0.0012	7.6280	–5.1445	0.0114	1200.0	98.5
2458173.708741	2.3572	0.0007	HARPS	0.0021	7.6307	–5.1614	0.0109	1200.0	109.6
2458173.722838	2.3569	0.0007	HARPS	0.0035	7.6322	–5.1469	0.0104	1200.0	114.9
2458173.737224	2.3584	0.0007	HARPS	–0.0001	7.6276	–5.1525	0.0112	1200.0	105.4
2458173.751472	2.3584	0.0007	HARPS	0.0020	7.6255	–5.1277	0.0103	1200.0	111.3
2458173.765569	2.3575	0.0007	HARPS	0.0015	7.6329	–5.1554	0.0115	1200.0	110.8
2458173.779956	2.3572	0.0006	HARPS	0.0055	7.6286	–5.1393	0.0106	1200.0	119.4
2458173.794064	2.3565	0.0006	HARPS	0.0024	7.6305	–5.1532	0.0111	1200.0	123.7
2458173.808312	2.3547	0.0006	HARPS	0.0020	7.6343	–5.1235	0.0103	1200.0	126.9
2458173.822560	2.3564	0.0006	HARPS	0.0045	7.6294	–5.1662	0.0118	1200.0	125.2
2458173.836668	2.3574	0.0007	HARPS	0.0026	7.6311	–5.1369	0.0123	1200.0	120.6
2458173.851043	2.3575	0.0007	HARPS	0.0026	7.6329	–5.1972	0.0160	1200.0	112.4
2458174.597927	2.3492	0.0008	HARPS	0.0039	7.6338	–5.1507	0.0107	1200.0	98.9
2458174.777961	2.3516	0.0008	HARPS	0.0013	7.6273	–5.1582	0.0140	900.0	97.1
2458175.607320	2.3460	0.0007	HARPS	0.0018	7.6323	–5.1414	0.0093	1200.0	104.7
2458175.749923	2.3485	0.0008	HARPS	0.0023	7.6315	–5.1476	0.0135	900.0	102.5
2458175.829842	2.3482	0.0008	HARPS	0.0016	7.6325	–5.2029	0.0185	1080.0	103.6
2458191.610255	2.3531	0.0009	HARPS	0.0060	7.6351	–5.0850	0.0107	900.0	86.8
2458192.599492	2.3558	0.0008	HARPS	0.0006	7.6352	–5.0962	0.0108	1050.0	87.4
2458193.575951	2.3608	0.0008	HARPS	–0.0022	7.6356	–5.0926	0.0099	900.0	87.7
2458194.585844	2.3620	0.0009	HARPS	–0.0017	7.6296	–5.1048	0.0115	900.0	82.8
2458195.701147	2.3618	0.0009	HARPS	0.0027	7.6295	–5.0994	0.0140	900.0	80.4
2458196.675171	2.3580	0.0008	HARPS	–0.0010	7.6303	–5.1836	0.0142	900.0	90.4
2458113.602755	2.3502	0.0008	HARPS-N	–0.0029	7.6009	–5.1238	0.0108	1500.0	92.0
2458114.746684	2.3434	0.0009	HARPS-N	–0.0037	7.6015	–5.1046	0.0132	900.0	75.8
2458129.709781	2.3420	0.0006	HARPS-N	–0.0017	7.6067	–5.1241	0.0061	1800.0	124.5
2458140.557742	2.3349	0.0022	HARPS-N	–0.0057	7.6049	–5.0840	0.0655	1200.0	40.2
2458140.573703	2.3399	0.0028	HARPS-N	0.0026	7.6069	–5.0065	0.0626	1200.0	32.6
2458169.491793	2.3552	0.0011	HARPS-N	–0.0012	7.5808	–5.2133	0.0220	2400.0	68.5
2458169.559756	2.3553	0.0008	HARPS-N	–0.0026	7.5893	–5.1472	0.0113	2100.0	89.4
2458169.629247	2.3569	0.0007	HARPS-N	–0.0033	7.5862	–5.1628	0.0099	2100.0	98.9

Table A1 – *continued*

Time [BJD]	RV [km s ⁻¹]	σ_{RV} [km s ⁻¹]	Ins.	BIS [km s ⁻¹]	FWHM [km s ⁻¹]	logRHK	$\sigma(\logRHK)$	t_{exp}	SNR ⁽¹⁾
2458171.549472	2.3625	0.0006	HARPS-N	−0.0000	7.5877	−5.1531	0.0066	1500.0	123.1
2458171.588592	2.3632	0.0005	HARPS-N	−0.0019	7.5879	−5.1311	0.0054	1500.0	133.5
2458201.362286	2.3370	0.0014	HARPS-N	−0.0017	7.5874	−5.2441	0.0365	1800.0	56.5
2458203.651234	2.3472	0.0027	HARPS-N	−0.0080	7.5902	— ⁽²⁾	— ⁽²⁾	1200.0	33.9

Table A2. A list of all detected oscillation frequencies and their uncertainties, derived according to the Bayesian method and using the MAP algorithm (see Section 3.3), together with their radial order and angular degree.

Order	Degree	Freq. (Bayes) [μHz]	$\sigma + \text{freq. Bayes}$ [μHz]	Freq. (MAP) [μHz]	$\sigma_{\text{freq., MAP}}$ [μHz]
14	0			1036.81	0.72
14	1			1065.09	0.66
14	2			1097.22	0.85
15	0			1104.12	0.65
15	1			1131.34	0.51
15	2	1162.99	0.46	1163.14	0.25
16	0	1168.60	0.19	1168.64	0.18
16	1	1197.36	0.20	1197.30	0.17
16	2	1230.81	0.28	1230.60	0.27
17	0	1236.03	0.96	1235.92	0.30
17	1	1264.61	0.18	1264.83	0.14
17	2	1299.19	0.29	1299.27	0.27
18	0	1303.64	0.21	1303.58	0.24
18	1	1332.55	0.19	1332.56	0.17
18	2	1366.61	0.49	1366.70	0.38
19	0	1370.87	0.28	1370.98	0.37
19	1	1399.62	0.30	1399.59	0.21
19	2	1433.46	0.51	1433.56	0.33
20	0	1438.52	0.50	1438.68	0.32
20	1	1466.49	0.36	1466.75	0.29
20	2	1502.42	1.1	1503.12	0.63
21	0	1506.45	0.26	1506.34	0.39
21	1	1534.18	0.30	1534.50	0.46
21	2			1569.65	1.29
22	0			1575.00	1.02

²²*Astrobiology Center, NINS, 2-21-1 Osawa, Mitaka, Tokyo 181-8588, Japan*²³*European Southern Observatory, Alonso de Córdova 3107, Vitacura, Casilla, 19001 Santiago de Chile, Chile*This paper has been typeset from a \LaTeX file prepared by the author.